Research article

Mesoscopic glass transition model: Influence of the cooling rate on the structure refinement

Vladimir Ankudinov, Konstantin Shklyaev and Mikhail Vasin*

Vereshchagin Institute of High Pressure Physics, Russian Academy of Sciences, 108840 Moscow, Russia

* **Correspondence:** Email: dr_vasin@mail.ru.

Abstract: The process of glass transition during the quenching in the domain with the cold wall has been numerically simulated. We have implemented the temperature-dependent form of the previously proposed theoretical model, which combined the heat transfer in the domain and the gauge theory of glass transition, assuming the presence of topologically stable distortions (disclinations) in the forming solid. The competition between crystallization (formation of polycrystalline structure) and the formation of the amorphous disordered phase has been shown. At the relatively slow cooling rates corresponding to the formation of the crystalline phase, we observed a columnar to equiaxed transition qualitatively similar to the observed in many metallic alloys. The moving front followed the equilibrium isotherm corresponding to the equilibrium temperature of transition in the disclinations subsystem, although front drag resulted in the effect of kinetic undercooling and the emergence of the maximum velocity of the crystallization front. High thermal conductivity values associated with the substantial heat flux lead to the bulk amorphous state. The dynamics of the coarsening of the primary amorphous structure depended on the annealing temperature.

Keywords: glass transition; quenching; gauge theory; heat transfer; solidification; amorphization; crystallization; phase field
Mathematics Subject Classification: 82-XX, 82Cxx, 82B26

1. Introduction

The development of the thermodynamically based calculation methods consisting of the solution of the heat and mass transfer equations with the phase evolution equations has made significant progress in the creation of the production technologies for metallic alloys with specific properties [1,2]. Despite significant progress, the study and description of the fundamental physical processes that occur during solidification remains a relevant and important task of modern condensed matter physics [3–6].

Modern technologies of the processing of metals and their alloys allow us to achieve experimentally significant undercoolings, temperature, and concentration gradients, and, as a result, rapid boundary interfaces [1]. Under such specific conditions, a liquid can solidify not only into an equilibrium phase, but also into a metastable crystalline, or into an amorphous metallic glass state. Experimental results present, that such mixed states can significantly improve the physical properties of materials [7]. Difficulties of describing such effects are related to the lack of understanding of the physics of the glass transition [8, 9], as well as to the difficulty of going beyond the equilibrium statistical physics. The latter is a consequence of the ergodicity violation of the amorphous melt due to the structural frustration [10, 11].

In this paper, we have tried to overcome these difficulties using the gauge theory of glass transition [12], which considers topologically stable distortions in forming the partially ordered phase as structural units. It allows us to describe the liquid-glass transition using continuous field theory in the presence of the time-dependent temperature field. This approach will potentially benefit to the development of phase field theory for the glass-forming alloys.

The paper is organized as follows: (i) After the introduction in Section 1.1, a brief review of the existing approaches of modeling amorphization and vitrification in the phase field method is given; (ii) the assumptions of the theoretical model considering the topologically protected perturbations as the main structural elements are formulated in Sections 2.1 and 2.2; (iii) the system of differential equations, considering the heat transfer is derived, and its numerical implementation is described in Sections 3.1 and 3.2; (iv) in Sections 3.3, we outline the details of the performed simulations and their relation to the real experiments; (v) results and discussion are summarized in Section 4. We discuss each set of simulations sequentially: Section 4.1—annealing from the disordered state at a constant temperature gradient for a certain time; Section 4.2—effect of changing of the shear modulus and variable thermal conductivity coefficient of heat transfer equation on the final structure, and correlation functions; Section 4.3—effect of the cooling rate fixed in time and varied along the x-axis and its qualitative influence on the final structure obtained after solidification; (vi) conclusions in Section 5 outline the obtained results.

1.1. Amorphization and vitrification in phase field models

The phase field (PF) and phase field crystal (PFC) methods [2] are widely introduced in materials science, in fact, they can be considered as a generalization of the mean-field approximation of the phase transitions theory [13–15]. The combination of these methods with nonequilibrium thermodynamics allows one to successfully describe rapid first order phase transitions [16, 17]. The PF also links the nano- and mesoscopic levels for the description of the structural changes [18, 19]. The fundamental challenges of the PF and PFC methods have either been resolved or, at least, are clear [20–22]. However, their application to the formation of non-ergodic amorphous phases has not been thoroughly investigated, since it requires going beyond the approximation of the mean field.

The application of such models to the non-ergodic amorphous phase states is not yet entirely clarified, since it requires a description of the separate ordering field corresponding to the glassy state, which in the general case must take into account the thermal conditions. The multi-scale combination of the thermodynamic approach with the microscopic dynamics of the particles (or defects) driven by the fluctuations is a known problem partially solved with the Smoluchowski equation [23,24]; however, it faces significant difficulties in accurate temperature accounting [25]. In particular, an attempt to

describe the transition to a glass-like state using the PFC method was made in [26–28] for pure single component systems, and the manuscript presents the formation of fine-grained glass-like structure at high cooling rates. One can observe the sequential delayed crystallization (and recrystallization) from amorphous nuclei to the crystalline bulk in PFC [29, 30]. In [31, 32], a hybrid model consisting of a combination of a continuous mean-field model and a multiphase PF model was developed. There, the liquid-glass transition was considered as a noise-induced structural relaxation, taking into account the phase-interface slowdown.

The transition to a glass-like state can be carried out using the kinetic models for diffusion coefficients as made in [33–35] with the PF model for single-component and binary systems; in these works the glass-forming phase is considered as a bulk phase with a low diffusion strongly dependent on temperature. However, this model did not take into account the frustration, and non-ergodic effects inherent in glass, which are necessary to describe the formation of a fine-grained glass-like structure at high cooling rates. In a number of papers, disordered amorphous phases are considered as analogues of liquids, where crystallization (phase transition) is the same as the transition from liquid or amorphous phase and corresponds to the first order phase transition [36, 37].

In [38–40], the glass transition was considered as a full-fledged phase transition, and the parameters of glassy state are considered in a bulk using the thermodynamic data obtained experimentally or with several approximations. One can supply the possessed challenges with some additional problems arising from the glass-liquid-solid interfaces description [32, 41], confined amorphous states [42], and from the presence of the long-time relaxations leading to a nonlinear mobility of the glass-forming alloys [43].

The PF-models usually operate with the scalar order parameters, but the glass transition introduces the infinite landscape of the possible metastable states, which can be introduced by the uncertainty of the direction of the vector order parameter. In the present work, we do not pretend to the new phase-field interpretation, although there is a possible benefit in addition to the PF-method such as a continuous model of the kinetically sensitive glass formation model. We propose a new continuous model unifying the simultaneous description of kinetically sensitive formation of crystalline and amorphous phases which, due to its simplicity, can significantly improve the PF-method in the description of non-ergodic effects of glass formation.

2. Gauge model of vitrification

2.1. Assumptions and model analysis

In order to create a phase-field model of the solidification process, with the competition between crystallization and vitrification, two main problems need to be solved: (i) The liquid-glass transition should be described; we propose such a description in terms of the field theory in the spirit of the fluctuation theory of phase transitions [44, 45], and we define the field of the "order" parameter corresponding to the glass state of matter; and (ii) the description should be coherent with the PF description of crystallization and imply the competition of these processes.

In our previous work, we proposed for this purpose the topological (or gauge) theory of the glass transition, developed in [12, 46]. In this theory, the glass transition is a phase transition in a system of topologically protected distortions (disclinations) in some locally ordered atomic structure. This theory has a long history, dating back to the 1970s and 1980s, and it describes the main properties of

glass transitions well. The idea of the theory was originally proposed by G. Toulouse [47] and has since been extended and refined by other researchers [48–56]. The glass transition in this case can be understood as a collective phenomenon involving the interactions between topological defects in a crystal lattice (the local order should not be necessarily crystalline). These defects are responsible for the structural disorder and mobility of particles in the glassy state, which are the key properties of glasses. This theory provides a useful framework for understanding the glass transition and its relationship to other physical phenomena such as plastic deformation, aging, and mechanical behavior. It describes all the characteristic properties of liquid-glass transitions, and also sheds light on the role of topological defects in other materials, such as polymers and colloids.

2.2. Model

We consider the liquid within the framework of Jacob Frenkel's conception, which is based on the similarity of the local structure of the liquid (within several coordination spheres) to the structure of the crystal at moderate temperatures [57]. This approach explains the similarity of many physical properties of matter in liquid and solid states observed on small spatial and temporal scales [58–65]. This concept is the basis of the field theories of glass transition, in which the glasses and undercooled liquids are considered as a locally ordered matter with a large number of topologically protected excitations (disclinations) [12, 51, 55, 56]. In fact, the disclinations act as the main structural elements, and the theory allows one to describe the number of important properties of the glass transition [12].

According to the Frenkel's approach, any liquid at the low temperatures has a local atomic order (at the distance of several coordination spheres), similar to that in a crystalline solid, or to an icosahedral noncrystalline ordering. Let one consider the simplest case with a single type of ordering, described by the order parameter $\mathbf{\Phi}$ [66]. When the temperature T is below certain critical value $T < T_c$, the field $\mathbf{\Phi}$ becomes nonzero in the considered domain, but the long-range order is absent because of the topologically protected excitations (disclinations). Thus, the fluid can be considered as an elastic medium in which both elastic and plastic deformations occur. The presence of the disclinations provides the fluidity of the substance, and elastic deformations determine a free energy $\mathcal{F}$ of the system, which can be written as follows:

$$\mathcal{F} = \frac{\lambda}{2} u_{ll}^2 + \mu \hat{\mathbf{u}}^2, \tag{2.1}$$

where λ is the bulk modulus, μ is the instantaneous shear modulus, and $\hat{\mathbf{u}} = u_{ij} = du_j/dx_i = \nabla_i u_j$ is the distortion tensor ($\mathbf{u}$ is the strain vector). Note that μ is a microscopic parameter. In the case of the observation times exceeding the short structural relaxation, the averaged (measured) static shear modulus is zero due to the presence of mobile plastic distortions in this system [12].

We consider a system in mechanical equilibrium, and $\mathbf{u}$-field is a free one. The elastic energy is away from the minimum of free energy landscape because the disordered structure is geometrically frustrated. Due to the frustration, $\mathbf{u}$-field contains stress regions caused by the topologically protected distortions. The topologically protected rotation distortions correspond to the disclinations (or vortex lines) [12]. The presence of the disclination breaks the connectivity of the space and leads to the appearance of an irreducible part in the distortion tensor corresponding to the rotation when moving around this disclination:

$$\oint \hat{\mathbf{u}} d\mathbf{l} = \int \nabla \times \hat{\mathbf{u}} \, d^2\mathbf{r} = \mathbf{\Omega} \delta_{\mathbf{r}=\mathbf{r}_n}^{(2)}, \tag{2.2}$$

where the space integration is performed over the dimensionless variable $|\mathbf{r}| < 1$: $V^{-1} \int dV = \int d^3\mathbf{r}$, and $\mathbf{\Omega}$ is the Frank pseudovector. The partition function of the system containing N disclinations can be represented in the form of the functional integral:

$$W = \int \mathcal{D}\hat{\mathbf{u}} \exp\left[-\beta \int d^3\mathbf{r}\,\mathcal{F}\right] \prod_{n=1}^{N} \delta\left(\nabla \times \hat{\mathbf{u}}_{\mathbf{r}_n} - \mathbf{\Omega} J_{\mathbf{r}_n}\right),$$

where $\beta = 1/(k_b T)$, $\delta(\ldots)$ is the functional delta-function, and $J_{\mathbf{r}} = \pm 1$ is a topological charge.

The partition function can be written as follows using the functional integral representation of the delta-function:

$$W = \int \mathcal{D}\hat{\mathbf{u}}\mathcal{D}\mathbf{A} \exp\left[-\beta \int d^3\mathbf{r}\left(\frac{1}{2}\mu\hat{\mathbf{u}}^2 + i\beta^{-1}\mathbf{A} \cdot \nabla \times \hat{\mathbf{u}} - \mathbf{A} \cdot \mathbf{\Omega} \sum_{n=1}^{N} J\delta_{\mathbf{r}=\mathbf{r}_n}^{(2)}\right)\right], \tag{2.3}$$

where $\mathbf{A}$ is an ancillary field, which follows the condition Eq (2.2), then following [12], one can consider the simplification where compressibility was neglected, so the rotation tensor is non-diagonal ($u_{ii} = 0$). After the integration over $\hat{\mathbf{u}}$-field, and averaging over the grand canonical ensemble of the vortices (see [12], Appendix I), the effective Hamiltonian density assumes the form:

$$\mathcal{H} = \frac{\beta^{-2}}{2\mu}(\nabla \times \mathbf{A})^2 - g\beta^{-1}\cos\left(\mathbf{\Omega}\mathbf{A}\right), \tag{2.4}$$

where g is the density of the vortex system. It is nothing else than the Hamiltonian density of the sine-Gordon theory [46, 67].

Such a topological system as described by Eqs (2.3) and (2.4) undergoes a phase transition [12] at the temperature T_g:

$$T_g = \frac{\mu}{k_b}\left(\frac{\Omega}{2\pi}\right)^2, \tag{2.5}$$

where Ω is equal to the Frank pseudovector modulus $\Omega = |\mathbf{\Omega}|$ [12]. Quantum-field theory suggests that, in the three-dimensional case, only the first four terms of the Taylor series expansion of the cosine function with respect to $\mathbf{A}$ are significant in the fluctuation region near the phase transition point [45]. It leads to the following effective Hamiltonian density form:

$$\mathcal{H} = \frac{\beta^{-2}}{2\mu}(\nabla \times \mathbf{A})^2 + M^2\left(\frac{1}{2}(\mathbf{\Omega}\mathbf{A})^2 - \frac{1}{4!}(\mathbf{\Omega}\mathbf{A})^4\right) + g\beta^{-1}\frac{\Omega^6}{6!}\mathbf{A}^6, \tag{2.6}$$

where $M^2 = g\Omega^2(T - T_g)$ is the square of the effective $\mathbf{A}$ field "mass".

The model describes a phase transition in a system of interacting topological defects (vortices), leading to the emergence of quasi-long-range order at finite temperature, corresponding to a vortex system with infinite correlation length. In such a model, one considers a topological phase transition, since it is defined by the topological properties of the system and cannot be explained by standard arguments. In [66] it was suggested that the $\nabla \times \mathbf{A}$ vector field could be used as an order parameter for such a transition. In order to define the physical meaning of this field, one follows the liquid state theory of Jakov Frenkel. We assume the presence of a local ordering in the liquid structure. In

this case, a long-range translational order is absent if the locally ordered clusters are disoriented with respect to each other. The absence of this disorientation corresponds to $\langle \hat{\mathbf{u}}^2 \rangle = 0$, which is equivalent to (see [66]):

$$\langle (\nabla \times \mathbf{A})^2 \rangle = 0. \tag{2.7}$$

It means the long-range crystalline ordering in the vicinity of the given point. Thus, $|\nabla \times \mathbf{A}|$ is the degree of distortion of the initial structural order at a given point, and the average of this value indicates the degree of disorder of the structure.

3. Dynamics

In our previous works [66, 68, 69], we considered some of the simplest cases, where the temperature field was homogeneous, and T was uniform throughout the domain. In the present study, we consider an inhomogeneous temperature distribution in the domain, with a continuous heat flux controlled manually or by solving the heat transfer equation. We assume that the phase transition in the subsystem of topological defects, corresponding to the glass transition, is accompanied by the release of a negligible amount of heat, and the temperature rate change is significantly higher than the rate of the structural changes. Therefore, we neglect the temperature change associated with this transition and focus only on the thermal fluctuations.

3.1. Equations of motion and heat transfer

Taking into account the presence of thermal fluctuations, the kinetics of the system with a non-conserving order parameter can be described in terms of stochastic nonequilibrium dynamics [44, 45, 70]. The following kinetic equations can be derived from the variational derivative of the full Hamiltonian Eq (2.6) with the addition of the stochastic source as $-\Gamma \partial_t \mathbf{A} = \delta \mathcal{H}/\delta \mathbf{A} + \beta^{-1}\xi$ [70]. Thus, the equation describing the dynamics of the $\mathbf{A}$-field can be written as a stochastic equation taking into account thermal fluctuations in the fluctuation region near the phase transition:

$$\begin{cases} \Gamma \dfrac{\partial \mathbf{A}}{\partial t} &= \dfrac{\beta^{-2}}{\gamma\mu}\nabla^2\mathbf{A} - g\Omega^2\mathbf{A}\left(\dfrac{1}{\beta} - \mu\left(\dfrac{\Omega}{2\pi}\right)^2\right)\left(1 - \dfrac{\Omega^2}{3!}|\mathbf{A}|^2\right) - \dfrac{g}{\beta}\mathbf{A}\dfrac{\Omega^6}{5!}|\mathbf{A}|^4 - \dfrac{\xi}{\beta}, \\ \dfrac{\partial T}{\partial t} &= k\nabla^2 T, \end{cases} \tag{3.1}$$

where γ is a phenomenological interfacial energy coefficient, and ξ is the dimensionless source of thermal fluctuations, which is the random variable with the normal distribution and unit variance. The local temperature value T obeys the heat transfer equation (or is specified by the given function $T(x, y, t)$ in the degenerate cases described below).

We consider the case of the local thermalization in the representative volumes with size $l \approx 50$, which is significantly larger than the size of the nodes ℓ exposed to the thermal fluctuations. We believe - that in the case of the absence of feedback from the $\mathbf{A}$-field equation to T, one can introduce the large-scale heat transfer equation as an external field Eq (3.1).

3.2. Numerical implementation

We have performed numerical simulations of the dynamical Eq (3.1), which was obtained with the Hamiltonian Eq (2.6) in the two-dimensional computational domain with the isolated (zero flux)

boundary conditions on **A**. In a general case, the three-dimensional case of such a system of equations can also be considered, however, the qualitative results are very similar to those obtained in the two-dimensional study. The symmetry of the system is reduced in Eq (2.3) and the continuous field formulation should not lead to unexpected effects in terms of sensitivity to the cooling kinetics.

The initial distribution was random with $|\mathbf{A}| = 1$. Such an initial distribution corresponds to the disordered liquid phase. The noise sources were obtained from the random function generator with the normal distribution and zero mean. The computational domains consisted of $L = 300 \times 300$ dimensionless units with up to 300 grid points along the edges; the maximum triangular mesh element size was set as $\ell = 1$. Provided in Table 1, parameters were used in most of the calculations. We tested the mesh and time-step convergence, and for the specific rates there were no significant influence on the size of the topological peculiarities or on the order parameter dynamics during the solidification process. The domain size was also sufficient to proceed to the formation of the bulk multigrain phase.

Table 1. The simulation parameters used for calculations.

Property	Value	Property	Value
μ, [J]	15.1	γ, [m^{-2}]	0.27
g, [–]	1	Ω, [–]	0.7
k_b, [J/K]	1	Γ, [s J]	1
$T_{initial}$, [K]	0.7	T_0, [K]	0.01
V_0, [K/s]	2×10^{-5}	V_1, [K s^{-1} m^{-1}]	4.5×10^{-6}
T_G, [K/m]	1×10^{-3}	k, [m^2 s^{-1}]	*variable*

To compute the given problem, we used the COMSOL Multiphysics 6.0 software [71] with PARDISO direct solver and the backward differentiation formula for time integration. The adaptive time step $\delta t = 1.0 \times 10^{-6}...1.0 \times 10^{1}$ was controlled at each step on convergence due to the presence of fluctuations and was fixed at the maximum value once the entire domain reached the target temperature T_1. All calculations were performed on a dual-processor AMD Epyc 7302-based computer.

3.3. Quenching simulations

The cold left domain wall simulates the case of ultrafast melt quenching (on the spinning drum), which is the most common experimental setup to produce glass from metallic melts [1, 7, 72, 73]. We considered the presented model which experiences bulk quenching with cooling rate equal to $V_{cool} = \partial_t T$ controlled by the heat transfer equation or an arbitrary function $T(x, y, t)$. The initial state corresponds to the disordered liquid with $|\mathbf{A}| = 1$ at the initial temperature $T = T_{initial} > T_g > T_0$. There are three different cases that have been introduced in the simulations performed:

- Section 4.1: Gradient temperature distribution $T = T_G x$, which was fixed in time during the simulation. No heat transfer equation was implemented in this case.
- Section 4.2: Solution of the heat transfer equation with the Dirichlet boundary condition $T = T_0$ at the left domain wall, $x = 0$, with different thermal conductivity k (see Eq (3.1)). Initial T values were set as $T = T_{initial}$.
- Section 4.3: Initial T was constant $T_{initial}$, then the domain was continuously cooled down with the

prescribed $V_{cool} = V_0 + V_1 x$ at $x = [0..L]$, till $T = T_0$. No heat transfer equation was implemented in this case.

The structural state of the system is characterized by the distortion correlation function $\langle \hat{\mathbf{u}}\hat{\mathbf{u}} \rangle \propto \langle (\nabla \times \mathbf{A})^2 \rangle$ [66, 69].

To analyze the time correlations in the domain, let one introduce the time-correlation function $G_t[f(\mathbf{r}, t)]$ which denotes the simple time correlation function in real space. It describes the spatio-temporal correlations of the given function $f(\mathbf{r}, t)$,

$$G_t[f, t] = \frac{1}{\tau_{max}} \int_0^{\tau_{max}} \int f(\mathbf{r}, \tau) f(\mathbf{r}, \tau + t) \mathrm{d}\mathbf{r}\mathrm{d}\tau, \tag{3.2}$$

where τ_{max} is the integration window chosen as half of the computation time $\tau_{max} = t_{max}/2$. In our study, we compute the correlations of the two-dimensional curl of $\mathbf{A}$-field for $f = (\nabla \times \mathbf{A})$, which is averaged over all $\mathbf{r}$ and corresponds to $\mathbf{k} = 0$ in the reciprocal space.

4. Results and discussion

4.1. Fixed gradient temperature distribution

The simulations performed (see Figure 1) allow one to define the structure selection depending on the final temperature distribution. The figures represent the gradual coarsening of the structure, which is different depending on the position in the domain and the corresponding T. Qualitatively similar structure selections depending on the different final temperatures performed at different cooling rates V_{cool} can be found in [74].
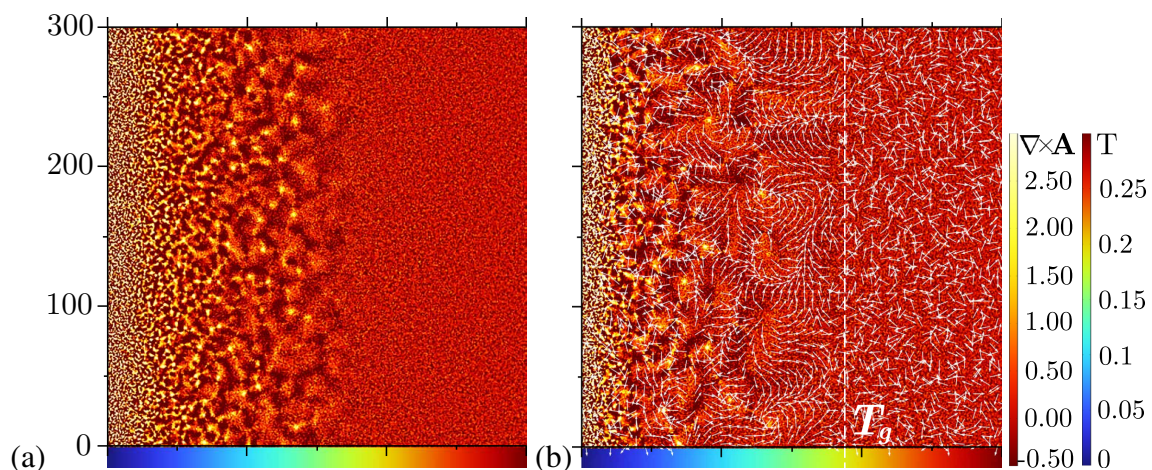

Figure 1. Relaxation of the order parameter $\nabla \times \mathbf{A}$ from the pure disordered state in the presence of the static temperature gradient $T = T_G x$ (temperature distribution T is shown in compact scale below the domain, distribution over the y-axis is constant): (a) $t = 1000$, (b) $t = 7500$. Panel (b) also shows the T_g isotherm and vector field $\mathbf{A}$, corresponding to the stress distribution.

For the temperatures $T < 0.02$, the amorphous phase appears on the left side of the domain $x \in [0..20]$ in the cold region, containing the structural inhomogeneities with the size around $q \approx 0.2$. This region is preserved at the very cold temperatures and correspondingly low fluctuations, which cannot have any observed effect on the further coarsening of the structure. Following to the right side, to the higher temperature region, the transition zone can be found at $x \in [20..40]$, which is characterized by the varying inhomogeneities of size $q \approx 5$ corresponding to the relatively stable fine-grained amorphous phase, which stays at $T < 0.04$ and experiences some coarsening up to $q \approx 8$, conditioned mainly by the ratio of surface and volume energy, resulting in the relatively stable microstructure. The fine polycrystalline structure can be observed from $x \in [40..120]$ at the later stages of the structure relaxation. This structure is formed from the coarse amorphous phase (can be seen in Figure 1(a)) during the annealing, which is mainly driven by the stochastic fluctuations of the **A**-field. The central zone $x \in [120..180]$ is filled with the crystalline phase with the relatively large size of grains $q \approx 50$ growing from the coarse polycrystalline structure (see Figure 1(a)) with multiple nuclei. These oriented crystals contain a tiny amount of defects. The formation of the large crystals occurs mostly at $t \in 2500..5000$ after the primary coarsening. The phase boundary is located at $x = 187$ at $T = T_g = 0.187$, which is the equilibrium transition temperature T_g. The phase to the right of the $x > 187$ region corresponds to the liquid at high $T > T_g$.

4.2. Influence of the finite thermal conductivity coefficient

To study the influence of the cooling with the varying heat flux controlled by the unsteady heat transfer equation, Eq (3.1), on the final microstructure, we performed a series of simulations with different heat transfer coefficients k. The Dirichlet boundary condition $T = T_0$ applied to the left domain wall allows one to model the case where the cold wall is in contact with the cooling reservoir as in rapid melt spinning experiments with the large cooled spinning drum. The thermal conductivity k here controls the total heat flow through the melt.

4.2.1. Effect of shear modulus

One can distinguish between the formation of the columnar crystals with the cross-section size $Q \approx 45$ in the slow cooling regime, at $k = 5$, which is presented in Figure 2. The left domain wall has cooled, becoming a region of the heterogeneous nucleation. The crystal boundary follows the isotherm $T = 0.165$, which corresponds to the effective temperature of the phase transition in the A-subsystem. The resulting temperature on the front is lower than the equilibrium one $T_g = 0.187$ observed in the case of the fixed temperature gradient (see Section 4.1, Figure 1). During the later cooling (see Figure 2(b)), the structure shows the result of the homogeneous nucleation and sequential polycrystalline growth. The ordered islands of the significant size $q \approx 32 - 45$ are comparable to the cross-section of columnar crystallites formed during the slow cooling and can be considered as equiaxed crystals forming polycrystalline aggregates. In our case, such polycrystalline structure resulted from the bulk relaxation on the later stages of the cooling. During the process of microstructure formation, the following stages are observed: (i) Emergence of fine amorphous structure after cooling below T_g, (ii) coarsening of the fine structure under the conditions of relatively high thermal fluctuations (corresponding to the annealing at $\approx 0.7 - 0.8 T_g$), and (iii) ordering and consolidation of adjacent regions and migration of defects to the grain boundaries.
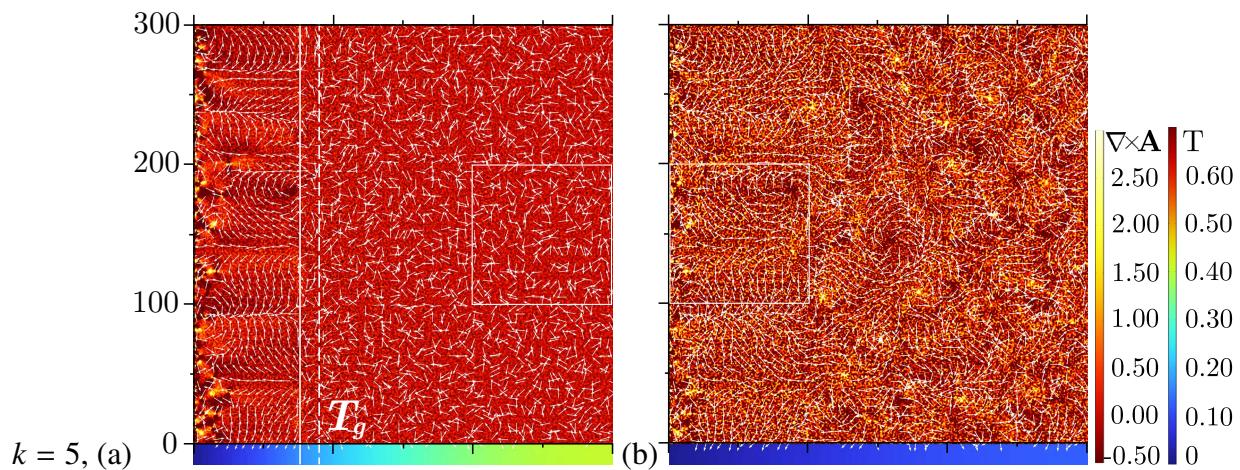
Figure 2. Evolution of the order parameter $\nabla \times \mathbf{A}$ during the cooling with the thermal conductivity $k = 5$, (temperature distribution T is shown in compact scale below the domain, distribution over the y-axis is constant): (a) $t = 5750$, (b) $t = 15000$. The snapshots also show the vector field $\mathbf{A}$, corresponding to the stress distribution. Panel (a) includes isotherm $T = 0.165$ corresponding to the solidification front (solid line) and dashed T_g.

The T_g isotherm accelerates to the right side of the domain, leading to the columnar to equiaxed transition (similar to that observed during the crystallization in the many metallic alloys [75, 76]). The effect of the limitation of the crystallization front propagation velocity is caused by the finite velocity of the reconfiguration of the $\mathbf{A}$-field, which is controlled by the $\Gamma_{\mathbf{A}}$ coefficient. In the simulations here we found that the transition to the bulk crystallization occurs at $t \approx 8000$ and the front position up to this time can be interpolated by the 2nd-order polynomial: $X = 7 \times 10^{-7} t^2 + 2.7 \times 10^{-3} t + 35.375$, so the maximum front propagation velocity is $V_{max} = 0.0139$ dimensionless units.

Note that μ is a microscopic parameter that is not zero in the liquid state. It corresponds to the macroscopic shear modulus in the case when the relaxation time of the structural system significantly exceeds the observation time. Usually, the shear modulus is inversely related to the temperature. Here, in our model μ controls the strain (inverse surface energy) of the $\mathbf{A}$-field, and for the convenience we assign the additional parameter γ for the precise selection of the ratio of the equilibrium transition temperature to the surface energy generated by the inhomogeneities of $\mathbf{A}$. To demonstrate the effect of the increasing $\gamma = 1$, one can refer to Figure 3, where for the low diffusivity coefficients $k = 1, 5$, the formation of the elongated crystals stops at once. The shear modulus leads to the disordered crystal growth Figure 3(a). Comparing the columnar growth with the same $k = 5$ from Figure 2(a) to Figure 3(b), there's a huge difference: Although the T_g and the kinetic undercooling are the same, the structure is significantly grained. The shear modulus value directly influences the minimum possible grinding curvature as a surface energy factor.
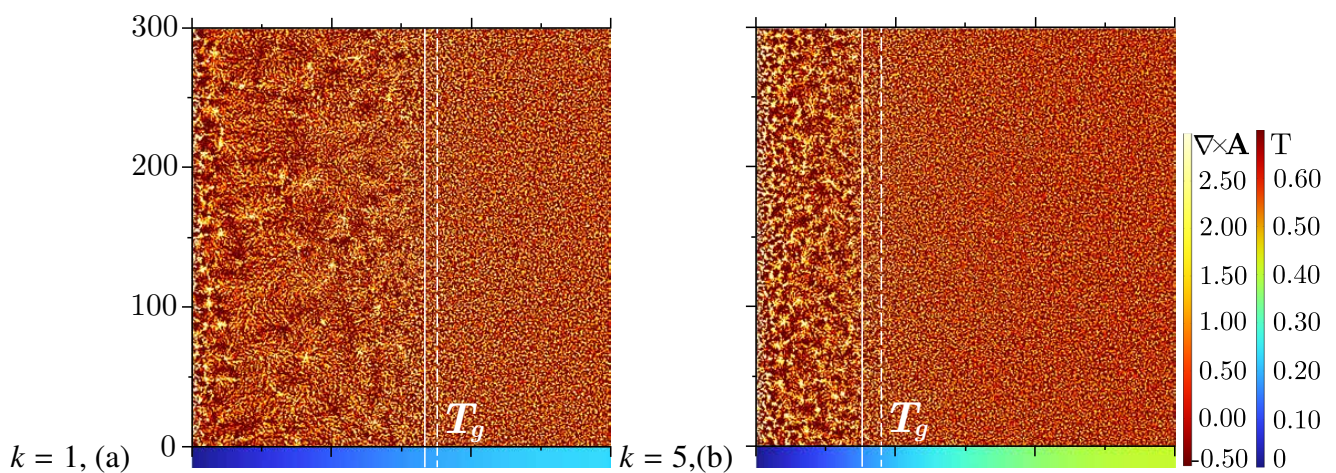
Figure 3. Evolution of the order parameter $\nabla \times \mathbf{A}$ during the cooling with the interfacial energy coefficient $\gamma = 1$ and different thermal conductivities (temperature distribution T is shown in compact scale below the domain, distribution over the y-axis is constant): (a) $k = 1$, $t = 50000$, (b) $k = 5$, $t = 5750$. The dashed isotherm $T_g = 0.165$ and the solid line corresponding to the solidification front are also shown.

4.2.2. Effect of the thermal conductivity coefficient

Figure 4 shows the intermediate stages and the final structures after the cooling with $k = 10$ (Figure 4(a),(b)), and $k = 20$ (Figure 4(c),(d)). Due to the simple T distribution, which is very close to the $erfc()$ solution of the heat transfer equation [77] in semi-infinite media, the right side of the domain experiences slower cooling rates in the later stages. However, the intermediate zone of the domain, $x \in [30..150]$, is subject to longer heat exposure and, hence, structural relaxation. One can distinguish (see Figure 4(a)) between the formation of the large polycrystalline structure with the sizes of around $q \approx 32$. Here, the local cooling rates are comparable to those in the $k = 5$ case. However, the right panel Figure 4(b) shows the slight coarsening of the structure in the intermediate region $x \in [30..150]$ up to $q \approx 35$. The gradient of the properties in the case $k = 10$, Figure 4(b) is caused by the long heat exposure (when $T \in [T_0..T_g]$) in the intermediate zone before the final freezing of the structure. The left panel of Figure 4(c), $k = 20$, shows the propagation of fine amorphous structure $q \approx 7$ (transition zone is blurred) into the liquid, which is relatively fast cooled, and thus forms the relaxed amorphous structure of $q \approx 20$ shown in Figure 4(d). One can still find the narrow zone $x \in [50..130]$ of the coarsened intermediate structure in Figure 4(d) with $q \approx 28$, but its boundaries are blurred. The effect of the crystallization front drag and transition to the vitrification (similar to that observed during the solidification of Cu-Zr [34, 35]) here can be observed here on the small grains on the left side of the domain Figure 4(c), which later appeared coarsened in the Figure 4(d) due to the subsequent slow relaxation. The interesting feature of the final structures in Figure 4(b),(d) is the presence of the distinguished elongated defect chains.
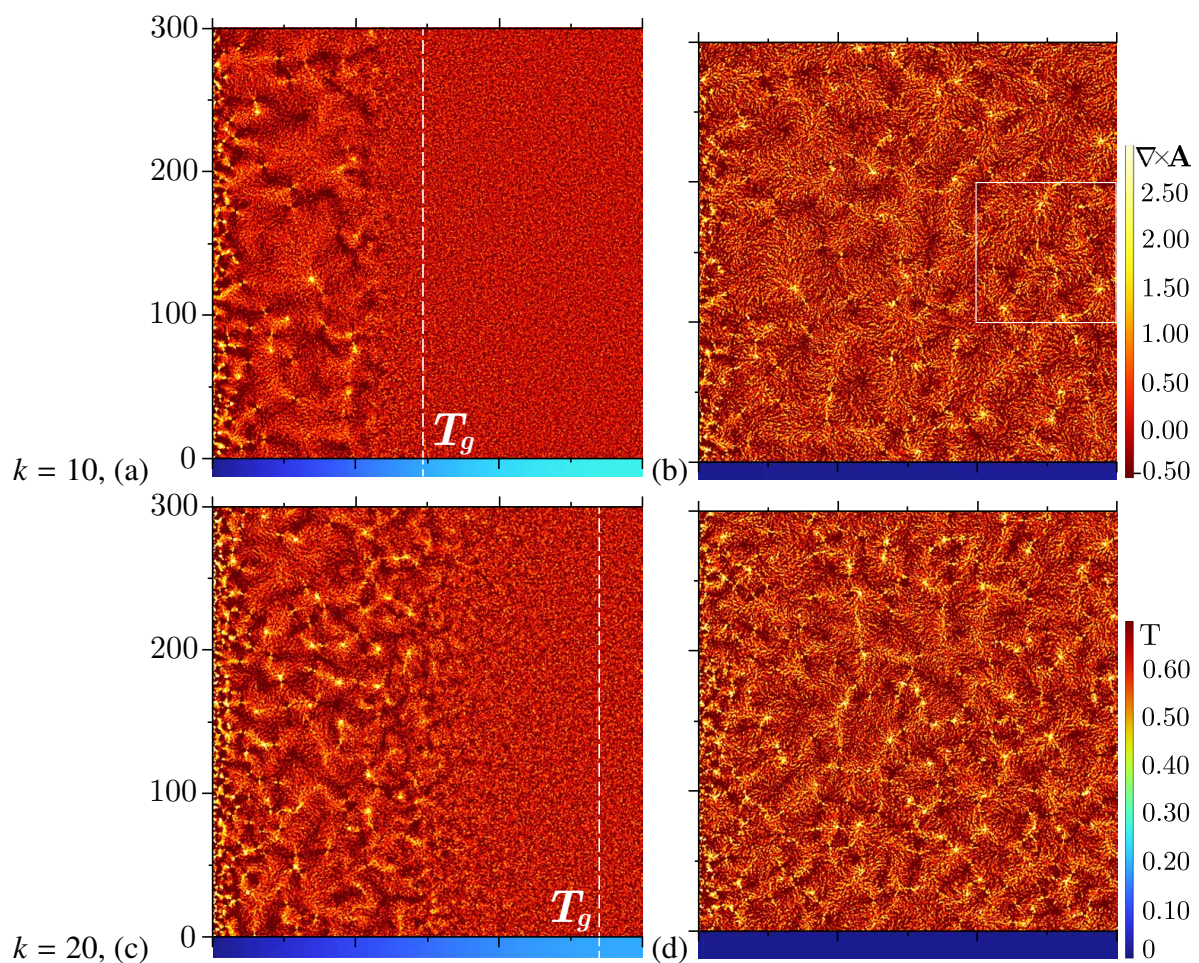
Figure 4. Evolution of the order parameter $\nabla \times \mathbf{A}$ during the cooling with the different thermal conductivity values: Upper panels (a) and (b) $k = 10$; lower panels (c) and (d) $k = 20$ (T is shown in compact scale below the domain, distribution over the y-axis is constant). Snapshots are given at the representative times: $k = 10$: (a) $t = 4500$, (b) $t = 20000$; $k = 20$: (c) $t = 2900$, (d) $t = 20000$. The dashed line in panels (a) and (c) corresponds to the isotherm T_g.

The almost instantaneous solidification (finished in the whole domain in $\Delta t \approx 1750$) occurred during the cooling with the thermal conductivity $k = 50$, see Figure 5. In Figure 5(a), the front of the amorphous phase can be clearly distinguished, while the phase front is rather blurred in present case ($\delta Z \approx 45$). After the transition to the $|\mathbf{A}| = const$ phase a gradual relaxation with coarsening from $q = 17$ to $q = 23$ was observed. After the relative long relaxation (around $\Delta t = 25000$), no further relaxation was observed. This can also be shown with the time correlation function $G_t(\nabla \times \mathbf{A})$ (see Figure 6). It should be noted that the final amorphous state of the disclination subsystem contains clusters that coalesce into a low-dimensional foam-like structure. The formation of such structures has often been observed in computer models of glasses (see, for example, [78]).
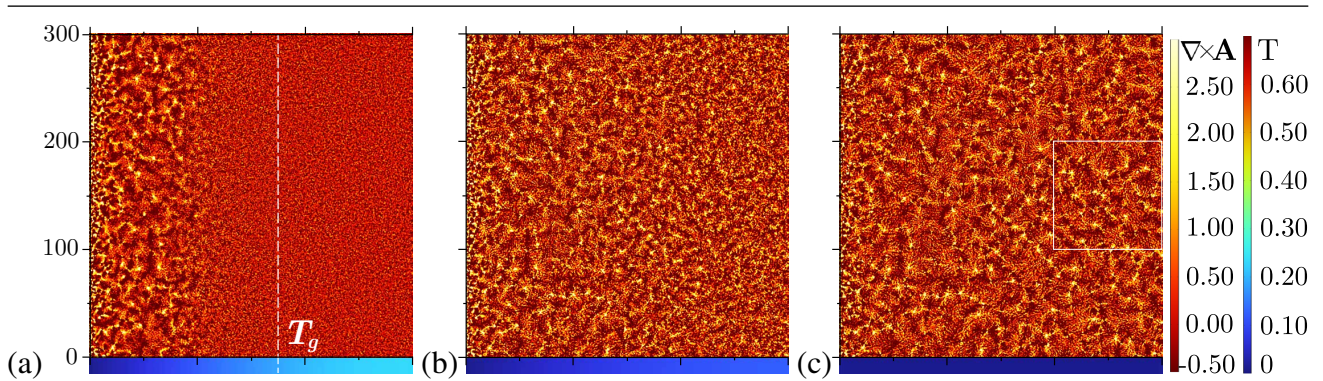
Figure 5. Coarsening of the structure represented by the order parameter $\nabla \times \mathbf{A}$ during the rapid cooling with $k = 50$ (T is shown in compact scale below the domain, distribution over the y-axis is constant). Snapshots are given at the representative times: (a) $t = 1000$; (b) $t = 1500$; (c) $t = 30000$. The dashed line in panel (a) corresponds to the isotherm T_g.
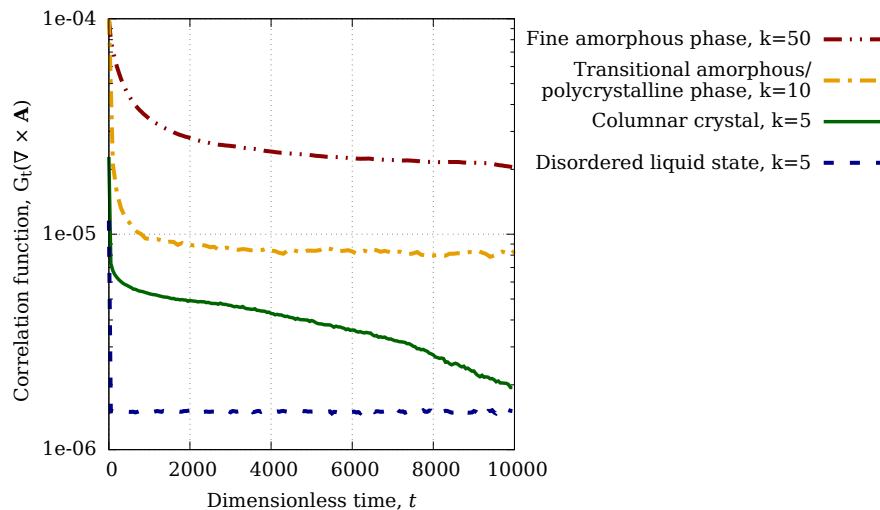

Figure 6. Correlation functions $G_t(\nabla \times \mathbf{A})$ for the subdomains containing certain phases: Fine amorphous Figure 5(c) for $k = 50$ (doble-dotted); transitional amorphous/polycrystalline structure Figure 4(b) for $k = 10$ (dash-dotted); columnar crystal Figure 2(b) for $k = 5$ (solid); liquid disordered phase Figure 2(a) for $k = 5$ (dashed). The subdomains are depicted on the correspondent figures with white frames. The curves were shifted down for the representative purposes.

Obtained distributions of structures from Figures 2–5 qualitatively correspond to the drums spinning at different speeds, and, thus, cooling rates [79] for Fe-Si-B [80], rare-element based alloys [81], Al-Si [82]. The columnar to equiaxed transition, Figure 2, is observed in spinning drum experiments with different materials such as Cu-P-Ni [83] and Co-based alloys [84], and the gradient properties were observed in experiments with Ni-based alloys [85] and coarsening in [86]. The effect of cooling rates are well studied for Fe-based ribbons [80, 87] and rare-element based alloys [81], and are also qualitatively reproduced by our model.

4.2.3. Time correlation function in subdomains

The time correlation functions $G_t(\nabla \times \mathbf{A})$, Eq (3.2), calculated for $t \in [0..10000]$, show different slopes of G_t for the amorphous and crystalline phases in the subdomains; see Figure 6. Here, the upper curve corresponds to the amorphous phase formed for $k = 50$; see Figure 5(c). The amorphous curve represents two different stages of relaxation (short-time and long-time) and crossover between them with shallow slope of the long-time correlations. The transition curve for $k = 10$ (see Figure 4(b)) represents the amorphous-like correlation in the fine-grained polycrystalline zone. The left part of the slowly cooled domain $k = 5$ with the oriented crystals shows the three-stage relaxation and a decrease of correlations on long timescales (see Figure 2). The right side of the domain $k = 5$ contains the liquid disordered phase and, hence, the absence of correlations. The total short-time correlations show an exponential relaxation associated to the mobility of the $\mathbf{A}$-field during primary cooling at $t \in [0..1000]$ in all solidified domains. The relaxation in the amorphized subdomain, Figure 6, is flatter due to the slowing down of the dynamics since the domain is at low T most of the time. The liquid disordered phase shows almost instantaneous relaxation.

4.3. Controlled cooling speed

The simulation with finite thermal conductivity values introduced earlier in Section 4.2 shows that the cooling rate of a local sample region depends on time and its spatial coordinates. In the current section, we have selected the most representative cooling rates and set the cooling rate at each point of the domain as $V_{cool}(x) = V_0 + V_1 x$ at $x = [0..L]$. The initial temperature was set as $T = T_{initial}$. The resulting microstructure of the solidified domain is shown in Figure 7(a). Here, one can see a pronounced effect of the V_{cool} on the final relaxed microstructure of the solidified domain. The cooling rate has a significant effect on the structure formation. Here, we obtain the gradient of simultaneously selected structures: From columnar crystals to polycrystalline and then to the amorphous structure, see Figure 7(a). With the cooling rate gradient, the whole range of the formed structures can coexist with each other at the low temperature (since they correspond to a single minimum of the free energy of the gauge parameter $\mathbf{A}$). The carried out numerical analysis of the kinetics of our model under the conditions of rapid quenching shows the qualitative agreement with the microstructures formed during rapid quenching [86, 88–90].
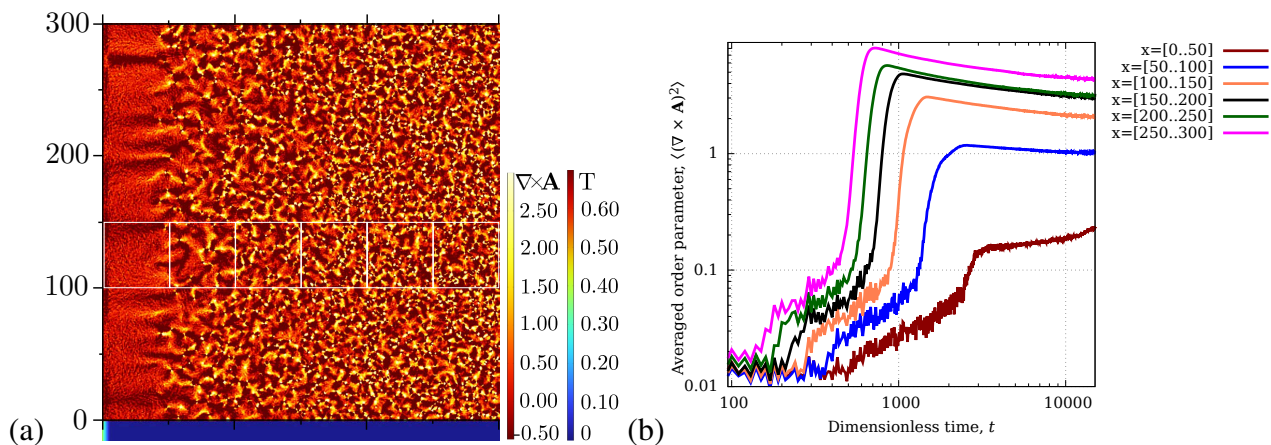
Figure 7. (a) Evolution of the order parameter $\nabla \times \mathbf{A}$ during the cooling with the controlled cooling rate $V_{cool} = V_0 + V_1 x$ at $x = [0..L]$, up to $T = T_0$ (T is shown in compact scale under the domain, distribution over the y-axis is constant). The snapshot is given after the relaxation $t = 15000$. White frames correspond to the subdomains of $\langle (\nabla \times \mathbf{A})^2 \rangle$ calculations. (b) Dependence of the averaged glass order parameter $\langle (\nabla \times \mathbf{A})^2 \rangle$ on t calculated in the subdomains.

A similar sensitivity to the cooling rate has been observed in previous studies of the gauge models of vitrification [66, 68, 69], although much smaller domains with full thermalization were considered. The distinction between crystalline and amorphous phases as final structures lies in the path to the final structure, which can be summarized as the evolution of the order parameter $\langle (\nabla \times \mathbf{A})^2 \rangle$ [66]. Previously, a hypothesis was proposed that the presence of a maximum on the $\langle (\nabla \times \mathbf{A})^2 \rangle_t$ evolution curve distinguished the presence of the amorphous state [66]. We assume that the glass transition occurs when the first derivative of the order parameter becomes zero as a result of the drastic change in kinetics from the critical to the relaxation regime. After the sharp increase up to the maximum value resulting from the glass transition, the order parameter for glass starts to decrease slowly as a result of aging. These differences are clearly visible in Figure 7(b), where x=[0..50] corresponds to the crystallized subdomain, x=[50..100] to the mixed/polycrystalline zone, and all other domains are vitrified. The higher value of the glass order parameter corresponds to a more amorphous system. The low magnitude of the averaged $\langle (\nabla \times \mathbf{A})^2 \rangle_t$ on the plateau (for later times, $t > 5000$) represents the presence of a small number of inhomogeneities and defects in the volume, which is typical for crystals with isolated defects or individual grains with pronounced boundaries.

5. Conclusions

The proposed model describes the solidification of the melt during the quenching simulations with a cold wall boundary condition, which is assumed to be in contact with the cooling reservoir as in rapid melt spinning experiments with the cooled drum. In the early stage, the solidification process starts with the formation of a fine-grained short-range ordering. Such local ordering is fragmented by the topologically protected excitations (disclinations), which prevent the formation of long-range translational order. The phase transition in the system of topologically protected excitations, which is implemented as the vector gauge field $\mathbf{A}$, was found to be sensitive to the local cooling rates, which are

directly related to heat fluxes and heat thermal conductivity coefficients.

Numerical simulations yielded the cooling rates corresponding to the competing regimes of crystal growth or amorphous phase formation. In the case of a high thermal conductivity $k => 20$ and, hence, high cooling rates, the domain solidifies into a bulk amorphous state with the emerging blurred transition zone revealing high magnitudes of the corresponding order parameter $\langle (\nabla \times \mathbf{A})^2 \rangle$. The structure corresponding to this state consists of a system of topological defects that tend to form low-dimensional clusters, forming a complex and disordered network. As the thermal conductivity of the material decreases $k <= 5$, a boundary between the polycrystalline and columnar crystal appears. The largest ordered (crystalline) columnar aggregate, where the field $(\nabla \times \mathbf{A})^2$ magnitude is small, has been observed for the case of slow solid-liquid front propagation. With the increased cooling rate and the corresponding increase of driving forces in the transition zone, we observed a columnar to equiaxed transition (CET) qualitatively similar to that observed in many metallic alloys [75, 76, 83, 84]. The moving front follows the equilibrium isotherm corresponding to the transition temperature T_g, although front drag leads to the effect of kinetic undercooling and the emergence of the crystallization front maximum velocity.

With the cooling rate gradient, a whole range of the formed structures can coexist with each other at the low temperature (since they correspond to a single minimum of the free energy of the gauge parameter $\mathbf{A}$). Nevertheless, even the fine-grained amorphous structure gradually coarsened up to the certain value $q \approx 23$, which was revealed during long simulations and corresponds to the magnitude of the parameter $\mu^{-1}\beta^{-2}$.

Despite the fact that we considered the simplest case, with a single ordering type, and corresponding topologically stable excitations, the model exhibited main characteristics typical for a glass-forming alloys. In particular, the behavior of this model showed competition between the vitrification and crystallization processes. The carried out numerical analysis of the kinetics of our model under the conditions of rapid quenching with simultaneous solution of the heat transfer and $\mathbf{A}$-field equations shows the qualitative agreement with the microstructures formed during rapid quenching in rapid melt spinning experiments [79–82, 85–87].

Appendix I

The effective Hamiltonian of our system is written as follows:

$$\mathcal{H} = \frac{\beta^{-2}}{2\mu}(\nabla \times \mathbf{A})^2 - i\beta^{-1}\mathbf{\Omega}\mathbf{A}\sum_{n=1}^{N}J\delta_{\mathbf{r}=\mathbf{r}_n}^{(2)}.$$

Carrying out the averaging over a grand canonical ensemble of the "particles" endowed with the two possible dimensionless charges $J_n = \pm 1$, there are possible vortices' configurations that can be taken into account. Then the path integral is as follows:

$$W = \int \mathcal{D}A \left\{ \exp\left[-\beta \int \mathrm{d}^3\mathbf{r} \frac{\beta^{-2}}{2\mu}(\nabla \times \mathbf{A})^2 \right] \times \sum_{N=1}^{\infty} \frac{(e^{-\beta\mathcal{E}_c})^N}{N!} \prod_{n=1}^{N} \int \mathrm{d}^3\mathbf{r}_n \sum_{J_n=\pm 1} \exp\left[iJ_n\mathbf{\Omega}\mathbf{A}(\mathbf{r}_n) \right] \right\}.$$

After summation, the effective Hamiltonian density takes the following form:

$$\mathcal{H} = \frac{\beta^{-2}}{2\mu}(\nabla \times \mathbf{A})^2 - g\beta^{-1}\cos(\mathbf{\Omega}\mathbf{A}),$$

where $g = e^{-\beta \mathcal{E}_c}$ is the density of vortices.

If one expands the cosine term into the power series, taking into account that in the 3D case only the first two terms of this expansion are relevant [12], then one obtains the following effective form of the Hamiltonian density:

$$\mathcal{H} = \frac{\beta^{-2}}{2\mu}(\nabla \times \mathbf{A})^2 + g\beta^{-1}(\mathbf{\Omega A})^2 \left(\frac{1}{2} - \frac{(\mathbf{\Omega A})^2}{4!} + \frac{(\mathbf{\Omega A})^4}{6!} \right).$$

One can represent the $\mathbf{A}$ field as the sum of fast, $\tilde{\mathbf{A}}$, and the slow, $\mathbf{A}$, parts if close to the critical point: $\mathbf{A} \rightarrow \mathbf{A} + \tilde{\mathbf{A}}$. After averaging over the fast field, the Hamiltonian density is written as follows:

$$\mathcal{H} = \frac{\beta^{-2}}{2\mu}(\nabla \times \mathbf{A})^2 + g\beta^{-1}\frac{\Omega^2}{2}\mathbf{A}^2 \left(1 - \frac{\Omega^2}{2}\langle \tilde{\mathbf{A}}\tilde{\mathbf{A}}\rangle_0 \right) - g\beta^{-1}\frac{\Omega^4}{4!}\mathbf{A}^4 \left(1 - \frac{\Omega^2}{2}\langle \tilde{\mathbf{A}}\tilde{\mathbf{A}}\rangle_0 \right) + g\beta^{-1}\frac{\Omega^6}{6!}\mathbf{A}^6, \quad (5.1)$$

where

$$\langle \tilde{\mathbf{A}}\tilde{\mathbf{A}}\rangle_0 = \int\limits_0^1 \frac{\mathrm{d}^3\mathbf{p}}{(2\pi)^3}\frac{\mu\beta}{\mathbf{p}^2} = \frac{\mu\beta}{2\pi^2}. \quad (5.2)$$

The shear modulus usually inversly depends on T. We assume that near the glass transition this dependence is a linear function: $\mu = \varepsilon(T_\mu - T)$, where T_μ is some temperature at which the shear elasticity appears in the liquid. Taking this into account, we lead to the following effective Hamiltonian density presentation:

$$\mathcal{H} = \frac{\beta^{-2}}{2\mu}(\nabla \times \mathbf{A})^2 + M^2 \left(\frac{1}{2}(\Omega \mathbf{A})^2 - \frac{1}{4!}(\Omega \mathbf{A})^4 \right) + g\beta^{-1}\frac{\Omega^6}{6!}\mathbf{A}^6, \quad (5.3)$$

where $M^2 = g\Omega^4\varepsilon(T - T_g)/(2\pi)^2$ is the square of the effective $\mathbf{A}$-field "mass", and

$$T_g = \frac{T_\mu}{1 + \dfrac{k_b}{\varepsilon}\left(\dfrac{2\pi}{\Omega}\right)^2} \quad (5.4)$$

is the phase transition temperature in the disclination subsystem. From above, the glass transition temperature is proportional to the shear modulus of the glass state, $T_g = \mu(T_g)(\Omega/2\pi)^2/k_b$. Thus, it is the well-determined thermodynamic value directly related to the elastic properties.

Author contributions

Use of AI tools declaration

The authors declare they have not used Artificial Intelligence (AI) tools in the creation of this article.

Acknowledgments

Conflict of interest

No potential conflict of interest was reported by the authors.

References

1. D. M. Herlach, P. K. Galenko, D. H. Moritz, *Metastable solids from undercooled melts*, Elsevier, 2007. https://doi.org/10.4028/www.scientific.net/MSF.539-543.1977

2. N. Provatas, K. Elder, *Phase-field methods in materials science and engineering*, Wiley-VCH, 2010.

3. M. I. Ojovan, Viscosity and glass transition in amorphous oxides, *Adv. Cond. Matter Phys.*, **2008** (2008), 817829. https://doi.org/10.1155/2008/817829

4. M. Sperl, E. Zaccarelli, F. Sciortino, P. Kumar, H. E. Stanley, Disconnected glass-glass transitions and diffusion anomalies in a model with two repulsive length scales, *Phys. Rev. Lett.*, **104** (2010), 145701. https://doi.org/10.1103/PhysRevLett.104.145701

5. L. Xu, S. V. Buldyrev, N. Giovambattista, H. E. Stanley, Liquid-liquid phase transition and glass transition in a monoatomic model system, *Int. J. Mol. Sci.*, **11** (2010), 5184–5200. https://doi.org/10.3390/ijms11125184

6. H. Tanaka, T. Kawasaki, H. Shintani, K. Watanabe, Critical-like behaviour of glass-forming liquids, *Nat. Mater.*, **9** (2010), 324–331. https://doi.org/10.1038/nmat2634 .

7. D. M. Herlach, Non-equilibrium solidification of undercooled metallic metls, *Mat. Sci. Eng. R*, **12** (1994), 177–272. https://doi.org/10.1016/0927-796X(94)90011-6

8. W. Gotze, L. Sjogren, Relaxation processes in supercooled liquids, *Rep. Prog. Phys.*, **55** (1992), 241–376. https://doi.org/10.1088/0034-4885/55/3/001

9. J. Jackle, Models of the glass transition, *Rep. Prog. Phys.*, **49** (1986), 171. https://dx.doi.org/10.1088/0034-4885/49/2/002

10. P. K. Galenko, D. Jou, Rapid solidification as non-ergodic phenomenon, *Phys. Rep.*, **818** (2019), 1–70. https://doi.org/10.1016/j.physrep.2019.06.002

11. R. E. Ryltsev, N. M. Chtchelkatchev, V. N. Ryzhov, Superfragile glassy dynamics of a one-component system with isotropic potential: Competition of diffusion and frustration, *Phys. Rev. Lett.*, **110** (2013), 025701. https://doi.org/10.1103/PhysRevLett.110.025701

12. M. G. Vasin, Glass transition as a topological phase transition, *Phys. Rev. E*, **106** (2022), 044124. https://doi.org/10.1103/PhysRevE.106.044124

13. E. Kats, V. Lebedev, A. Muratov, Weak crystallization theory, *Phys. Rep.*, **228** (1993), 1–91. https://doi.org/10.1016/0370-1573(93)90119-X

14. R. Prieler, D. Li, H. Emmerich, Nucleation and successive microstructure evolution via phase-field and phase-field crystal method, *J. Cryst. Growth*, **312** (2010), 1434–1436. http://dx.doi.org/10.1016/j.jcrysgro.2009.09.022

15. D. Tourret, H. Liu, J. LLorca, Phase-field modeling of microstructure evolution: Recent applications, perspectives and challenges, *Prog. Mater. Sci.*, **123** (2022), 100810. https://doi.org/10.1016/j.pmatsci.2021.100810

16. D. Jou, J. C. Vázquez, G. Lebon, *Extended irreversible thermodynamics*, 4 Eds., Springer Berlin Heidelberg, 2010. https://doi.org/10.1007/978-90-481-3074-0

17. P. Galenko, D. Jou, Diffuse-interface model for rapid phase transformations in nonequilibrium systems, *Phys. Rev. E*, **71** (2005), 046125. https://doi.org/10.1103/PhysRevE.71.046125

18. M. D. Krivilyov, E. V. Kharanzhevskii, V. G. Lebedev, D. A. Danilov, E. V. Danilova, P. K. Galenko, Synthesis of composite coatings using rapid laser sintering of metallic powder mixtures, *Phys. Met. Metallogr.+*, **114** (2013), 799–820. https://doi.org/10.1134/S0031918X13080073

19. H. Fu, M. Dehsara, M. Krivilyov, S. D. Mesarovic, D. P. Sekulic, Kinetics of the molten Al-Si triple line movement during a brazed joint formation, *J. Mater. Sci.*, **51** (2016), 1798–1812. https://doi.org/10.1007/s10853-015-9550-7

20. I. Steinbach, L. Zhang, M. Plapp, Phase-field model with finite interface dissipation, *Acta Mater.*, **60** (2012), 2689–2701. https://doi.org/10.1016/j.actamat.2012.01.035

21. H. Wang, P. K. Galenko, X. Zhang, W. Kuang, F. Liu, D. M. Herlach, Phase-field modeling of an abrupt disappearance of solute drag in rapid solidification, *Acta Mater.*, **90** (2015), 282–291. https://doi.org/10.1016/j.actamat.2015.02.021

22. D. A. Danilov, V. G. Lebedev, P. K. Galenko, A grand potential approach to phase-field modeling of rapid solidification, *J. Non-Equil. Thermody.*, **39** (2014), 93–111. https://doi.org/10.1515/jnetdy-2013-0032

23. U. M. B. Marconi, P. Tarazona, Dynamic density functional theory of fluids, *J. Chem. Phys.*, **110** (1999), 8032–8044. https://doi.org/10.1063/1.478705

24. S. Van Teeffelen, R. Backofen, A. Voigt, H. Löwen, Derivation of the phase-field-crystal model for colloidal solidification, *Phys. Rev. E*, **79** (2009), 1–10. https://doi.org/10.1103/PhysRevE.79.051404

25. V. Ankudinov, I. Starodumov, N. P. Kryuchkov, E. V. Yakovlev, S. O. Yurchenko, P. K. Galenko, Correlated noise effect on the structure formation in the phase-field crystal model, *Math. Method. Appl. Sci.*, **44** (2021), 12185–12193. https://doi.org/10.1002/mma.6887

26. J. Berry, K. R. Elder, M. Grant, Simulation of an atomistic dynamic field theory for monatomic liquids: Freezing and glass formation, *Phys. Rev. E*, **77** (2008), 061506. https://doi.org/10.1103/PhysRevE.77.061506

27. A. J. Archer, M. J. Robbins, U. Thiele, E. Knobloch, Solidification fronts in supercooled liquids: How rapid fronts can lead to disordered glassy solids, *Phys. Rev. E*, **86** (2012), 031603. https://doi.org/10.1103/PhysRevE.86.031603

28. J. Berry, M. Grant, Modeling multiple time scales during glass formation with phase-field crystals, *Phys. Rev. Lett.*, **106** (2011), 175702. https://doi.org/10.1103/PhysRevLett.106.175702

29. S. Abdalla, A. J. Archer, L. Gránásy, G. I. Tóth, Thermodynamics, formation dynamics, and structural correlations in the bulk amorphous phase of the phase-field crystal model, *J. Chem. Phys.*, **157** (2022), 164502. https://doi.org/10.1063/5.0114705

30. S. Tang, J. C. Wang, B. Svendsen, D. Raabe, Competitive bcc and fcc crystal nucleation from non-equilibrium liquids studied by phase-field crystal simulation, *Acta Mater.*, **139** (2017), 196–204. https://doi.org/10.1016/j.actamat.2017.08.015

31. T. Wang, E. Napolitano, A phase-field model for phase transformations in glass-forming alloys, *Metall. Mater. Trans. A*, **43** (2012), 2662–2668. https://doi.org/10.1007/s11661-012-1136-2

32. A. Ericsson, M. Fisk, H. Hallberg, Modeling of nucleation and growth in glass-forming alloys using a combination of classical and phase-field theory, *Comput. Mater. Sci.*, **165** (2019), 167–179. https://doi.org/10.1016/j.commatsci.2019.04.008

33. P. Bruna, E. Pineda, D. Crespo, Phase-field modeling of glass crystallization: Change of the transport properties and crystallization kinetic, *J. Non-Cryst. Solids*, **353** (2007), 1002–1004. https://doi.org/10.1016/j.jnoncrysol.2006.12.086

34. P. K. Galenko, V. Ankudinov, K. Reuther, M. Rettenmayr, A. Salhoumi, E. V. Kharanzhevskiy, Thermodynamics of rapid solidification and crystal growth kinetics in glass-forming alloys, *Philos. T. Roy. Soc. A*, **377** (2019), 20180205. https://doi.org/10.1098/rsta.2018.0205

35. P. K. Galenko, R. Wonneberger, S. Koch, V. Ankudinov, E. V. Kharanzhevskiy, M. Rettenmayr, Bell-shaped "dendrite velocity-undercooling" relationship with an abrupt drop of solidification kinetics in glass forming Cu-Zr(-Ni) melts, *J. Cryst. Growth*, **532** (2020), 125411. https://doi.org/10.1016/j.jcrysgro.2019.125411

36. M. V. Dudorov, A. D. Drozin, A. V. Stryukov, V. E. Roshchin, Mathematical model of solidification of melt with high-speed cooling, *J. Phys.-Condens. Mat.*, **34** (2022), 444002. https://doi.org/10.1088/1361-648X/ac8c12

37. P. A. Gamov, A. D. Drozin, M. V. Dudorov, V. E. Roshchin, Model for nanocrystal growth in an amorphous alloy, *Russ. Metall.+*, **2012** (2012), 1002–1005. https://doi.org/10.1134/S0036029512110055

38. M. M. A. Rafique, Modelling and simulation of solidification phenomena during additive manufacturing of bulk metallic glass matrix composites (BMGMC)—A brief review and introduction of technique, *J. Encapsulat. Adsorpt. Sci.*, **8** (2018), 67–116. https://doi.org/10.4236/jeas.2018.82005

39. X. H. Wu, G. Wang, D. C. Zeng, Z. W. Liu, Prediction of the glass-forming ability of Fe-B binary alloys based on a continuum-field-multi-phase-field model, *Comput. Mater. Sci.*, **108** (2015), 27–33. https://doi.org/10.1016/j.commatsci.2015.06.004

40. X. Wu, G. Wang, D. Zeng, Prediction of the glass forming ability in a Fe-25%B binary amorphous alloy based on phase-field method, *J. Non-Cryst. Solids*, **466–467** (2017), 52–57. https://doi.org/10.1016/j.jnoncrysol.2017.03.043

41. S. Ganorkar, Y. H. Lee, S. Lee, Y. C. Cho, T. Ishikawa, G. W. Lee, Unequal effect of

thermodynamics and kinetics on glass forming ability of Cu-Zr alloys, *AIP Adv.*, **10** (2020), 045114. https://doi.org/10.1063/5.0002784

42. C. Cammarota, G. Gradenigo, G. Biroli, Confinement as a tool to probe amorphous order, *Phys. Rev. Lett.*, **111** (2013), 1–5. https://doi.org/10.1103/PhysRevLett.111.107801

43. A. A. Novokreshchenova, V. G. Lebedev, Determining the phase-field mobility of pure nickel based on molecular dynamics data, *Tech. Phys.*, **62** (2017), 642–644. https://doi.org/10.1134/S1063784217040181

44. A. Z. Patashinskii, V. L. Pokrovskii, *Fluctuation theory of phase transitions*, Oxford/New York: Pergamon Press, 1979. http://doi.org/10.1002/bbpc.19800840723

45. A. N. Vasilev, *Quantum-field renormalization groups in the cases of critical-behavior and stochastical dynamics*, Russia: PIYAF Publ., Saint-Petersburg, 1998.

46. M. G. Vasin, V. M. Vinokur, Description of glass transition kinetics in 3D XY model in terms of gauge field theory, *Phys. A*, **525** (2019), 1161–1169. https://doi.org/10.1016/j.physa.2019.04.065

47. G. Toulouse, Theory of the frustration effect in spin glasses: I, *Commun. Phys.*, **2** (1977), 115–119.

48. J. C. Dyre, Colloquium: The glass transition and elastic models of glass-forming liquids, *Rev. Mod. Phys.*, **78** (2006), 953–972. https://doi.org/10.1103/RevModPhys.78.953

49. J. Villain, Two-level systems in a spin-glass model: II. Three-dimensional model and effect of a magnetic field, *J. Phys. C*, **11** (1978), 745. https://doi.org/10.1088/0022-3719/11/4/018

50. E. Fradkin, B. A. Huberman, S. H. Shenker, Gauge symmetries in random magnetic systems, *Phys. Rev. B*, **18** (1978), 4789–4814. https://link.aps.org/doi/10.1103/PhysRevB.18.4789

51. N. R. Blackett, Disclination lines in glasses, *Philos. Mag.*, **40** (1979), 859–868. https://doi.org/10.1080/01418617908234879

52. D. R. Nelson, Order, frustration, and defects in liquids and glasses, *Phys. Rev. B*, **28** (1983), 5515–5535. https://doi.org/10.1103/PhysRevB.28.5515

53. I. E. Dzyaloshinskii, G. E. Volovick, Poisson brackets in condensed matter physics, *Ann. Phys.*, **125** (1980), 67–97. https://doi.org/10.1016/0003-4916(80)90119-0

54. I. E. Dzyaloshinskii, S. P. Obukhov, Topological phase transition in the XY model of a spin glass, *Zh. Eksp. Teor. Fiz*, **83** (1982), 13–832.

55. M. Baggioli, I. Kriuchevskyi, T. W. Sirk, A. Zaccone, Plasticity in amorphous solids is mediated by topological defects in the displacement field, *Phys. Rev. Lett.*, **127** (2021), 015501. https://doi.org/10.1103/PhysRevLett.127.015501

56. M. Baggioli, M. Landry, A. Zaccone, Deformations, relaxation, and broken symmetries in liquids, solids, and glasses: A unified topological field theory, *Phys. Rev. E*, **105** (2022), 024602. https://doi.org/10.1103/PhysRevE.105.024602

57. J. Frenkel, *Kinetic theory of liquids*, Oxford: Oxford University Press, 1947.

58. M. Grimsditch, R. Bhadra, L. M. Torell, Shear waves through the glass-liquid transformation, *Phys. Rev. Lett.*, **62** (1989), 2616. https://doi.org/10.1103/PhysRevLett.62.2616

59. T. Pezeril, C. Klieber, S. Andrieu, K. A. Nelson, Optical generation of gigahertz-frequency shear acoustic waves in liquid glycerol, *Phys. Rev. Lett.*, **102** (2009), 107402. https://doi.org/10.1103/PhysRevLett.102.107402

60. Y. H. Jeong, S. R. Nagel, S. Bhattacharya, Ultrasonic investigation of the glass transition in glycerol, *Phys. Rev. A*, **34** (1986), 602. https://doi.org/10.1103/PhysRevA.34.602

61. S. Hosokawa, M. Inui, Y. Kajihara, K. Matsuda, T. Ichitsubo, W. C. Pilgrim, et al., Transverse acoustic excitations in liquid Ga, *Phys. Rev. Lett.*, **102** (2009), 105502. https://doi.org/10.1103/PhysRevLett.102.105502

62. V. M. Giordano, G. Monaco, Inelastic x-ray scattering study of liquid Ga: Implications for the short-range order, *Phys. Rev. B*, **84** (2011), 052201. https://doi.org/10.1103/PhysRevB.84.052201

63. T. Scopigno, G. Ruocco, F. Sette, Microscopic dynamics in liquid metals: The experimental point of view, *Rev. Mod. Phys.*, **77** (2005), 881–933. https://doi.org/10.1103/RevModPhys.77.881

64. E. Pontecorvo, M. Krisch, A. Cunsolo, G. Monaco, A. Mermet, R. Verbeni, et al., High-frequency longitudinal and transverse dynamics in water, *Phys. Rev. E*, **71** (2005), 011501. https://doi.org/10.1103/PhysRevE.71.011501

65. W. C. Pilgrim, C. Morkel, State dependent particle dynamics in liquid alkali metals, *J. Phys.-Condens. Mat.*, **18** (2006), R585. https://doi.org/10.1088/0953-8984/18/37/R01

66. M. G. Vasin, V. Ankudinov, Phase-field model of glass transition: Behavior under uniform quenching, *Phase Transit.*, 2024, 1–19. https://dx.doi.org/10.1080/01411594.2024.2353297

67. P. Minnhagen, The two-dimensional Coulomb gas, vortex unbinding, and superfluid-superconducting films, *Rev. Mod. Phys.*, **59** (1987), 1001. https://doi.org/10.1103/RevModPhys.59.1001

68. M. Vasin, V. Ankudinov, Soft model of solidification with the order-disorder states competition, *Math. Method. Appl. Sci.*, **45** (2022), 8082–8095. https://doi.org/10.1002/mma.8035

69. M. Vasin, V. Ankudinov, Competition of glass and crystal: Phase-field model, *Math. Method. Appl. Sci.*, **47** (2024), 6798–6809. https://doi.org/10.1002/mma.9207

70. P. C. Hohenberg, B. I. Halperin, Theory of dynamic critical phenomena, *Rev. Mod. Phys.*, **49** (1977), 435–479. https://doi.org/10.1103/RevModPhys.49.435

71. www.comsol.com, COMSOL Multiphysics® v.6.0, www.comsol.com, COMSOL AB, Stockholm, Sweden.

72. R. C. Budhani, T. C. Goel, K. L. Chopra, Melt-spinning technique for preparation of metallic glasses, *B. Mater. Sci.*, **4** (1982), 549–561. https://doi.org/10.1007/BF02824962

73. J. Schroers, Processing of bulk metallic glass, *Adv. Mater.*, **22** (2010), 1566–1597. https://doi.org/10.1002/adma.200902776

74. M. Vasin, V. Lebedev, V. Ankudinov, K. Shklyaev, The phase-field model of the glass transition, *Chem. Phys. Mesoscopy*, **25** (2023), 14. https://doi.org/10.15350/17270529.2023.4.46

75. P. A. Geslin, C. H. Chen, A. M. Tabrizi, A. Karma, Dendritic needle network modeling of the Columnar-to-Equiaxed transition. Part I: Two dimensional formulation and comparison with theory, *Acta Mater.*, **202** (2021), 42–54. https://doi.org/10.1016/j.actamat.2020.10.009

76. W. Kurz, C. Bezençon, M. Gäumann, Columnar to equiaxed transition in solidification processing, *Sci. Technol. Adv. Mat.*, **2** (2001), 185–191. https://doi.org/10.1016/S1468-6996(01)00047-X

77. B. R. Bird, E. S. Warren, N. E. Lightfoot, *Transport phenomena*, John Wiley & Sons, 2007.

78. Z. Wang, B. Riechers, P. M. Derlet, R. Maaß, Atomic cluster dynamics causes intermittent aging of metallic glasses, *Acta Mater.*, **267** (2024), 119730. https://doi.org/10.1016/j.actamat.2024.119730

79. V. I. Tkatch, A. M. Grishin, V. V. Maksimov, Estimation of the heat transfer coefficient in melt spinning process, *J. Phys.*, **144** (2009), 012104. https://doi.org/10.1088/1742-6596/144/1/012104

80. R. E. Napolitano, H. Meco, The role of melt pool behavior in free-jet melt spinning, *Metall. Mater. Trans. A*, **35 A** (2004), 1539–1553. https://doi.org/10.1007/s11661-004-0261-y

81. A. B. Lysenko, T. V. Kalinina, A. M. V. Tomina, Y. V. Vishnevskaya, O. Popil, *Production conditions and fine structure parameters of metallic glasses based on light rare-earth elements*, In: IOP Conference Series: Materials Science and Engineering, IOP Publishing, **1256** (2022), 012011. https://doi.org/10.1088/1757-899X/1256/1/012011

82. O. Gusakova, V. Shepelevich, D. Alexandrov, I. Starodumov, Rapid quenching effect on the microstructure of Al-Si eutectic Zn-doped alloy, *J. Cryst. Growth*, **531** (2020), 125333. https://doi.org/10.1016/j.jcrysgro.2019.125333 .

83. S. A. Tavolzhanskii, I. N. Pashkov, G. A. Aleksanyan, Analysis of the production of ribbons of Copper-Phosphorus solder by the lateral flow of a melt onto a rotating roller mold, *Metallurgist*, **59** (2016), 843–850. http://link.springer.com/10.1007/s11015-016-0182-1.

84. A. A. Shirzadi, T. Kozieł, G. Cios, P. Bała, Development of Auto Ejection Melt Spinning (AEMS) and its application in fabrication of cobalt-based ribbons, *J. Mater. Process. Tech.*, **264** (2019), 377–381. https://doi.org/10.1016/j.jmatprotec.2018.09.028

85. R. Prasad, G. Phanikumar, Martensite and nanocrystalline phase formation in rapidly solidified Ni_2MnGa alloy by melt-spinning, *Mater. Sci. Forum*, **649** (2010), 35–40. https://doi.org/10.4028/www.scientific.net/MSF.649.35

86. A. K. Demyanetz, M. Bamberger, M. Regev, Quantitative microstructure study of melt-spun $Mg_{65}Cu_{25}Y_{10}$, *SN Appl. Sci.*, **2** (2020), 1–10. https://doi.org/10.1007/s42452-020-03522-3

87. V. I. Tkatch, A. I. Limanovskii, S. N. Denisenko, S. G. Rassolov, The effect of the melt-spinning processing parameters on the rate of cooling, *Mater. Sci. Eng. A*, **323** (2002), 91–96. https://doi.org/10.1016/S0921-5093(01)01346-6

88. N. Liu, T. Ma, C. Liao, G. Liu, R. M. O. Mota, J. Liu, et al., Combinatorial measurement of critical cooling rates in aluminum-base metallic glass forming alloys, *Sci. Rep.*, **11** (2021), 3903. https://doi.org/10.1038/s41598-021-83384-w

89. H. Fiedler, H. Mühlbach, G. Stephani, The effect of the main processing parameters on the geometry of amorphous metal ribbons during planar flow casting (PFC), *J. Mater. Sci.*, **19** (1984), 3229–3235. https://doi.org/10.1007/BF00549809

90. H. S. Chen, C. E. Miller, Centrifugal spinning of metallic glass filaments, *Mater. Res. Bull.*, **11** (1976), 49–54. https://doi.org/10.1016/0025-5408(76)90213-0